Environmental Research 195 (2021) 110842

Contents lists available at ScienceDirect

Environmental Research

journal homepage: www.elsevier.com/locate/envres

Faster electron injection and higher interface reactivity in g-C_3N_4/Fe_2O_3 nanohybrid for efficient photo-Fenton-like activity toward antibiotics degradation

Hui Zhao [a,b], Cheng Tian [a], Jian Mei [a], Shijian Yang [a,*], Po Keung Wong [b,c,**]

[a] *Jiangsu Key Laboratory of Anaerobic Biotechnology, School of Environment and Civil Engineering, Jiangnan University, 1800 Lihu Avenue, Wuxi, 214122, China*
[b] *School of Life Sciences, The Chinese University of Hong Kong, Shatin, NT, Hong Kong SAR, China*
[c] *Institute of Environmental Health and Pollution Control, School of Environmental Science & Engineering, Guangdong University of Technology, Guangzhou, 510006, China*

ARTICLE INFO

Keywords:
g-C_3N_4/Fe_2O_3
Photo-Fenton
Structure-activity relationship
Electron transfer kinetics
Tetracycline removal

ABSTRACT

Two different morphologies of Fe_2O_3 involving nanodots and nanosheets were deposited on g-C_3N_4 nanosheets by simple *in-situ* deposition and impregnation-hydrothermal methods, respectively. Structural effect of Fe_2O_3 on photo-Fenton-like activity and charge transfer at the interface in these two g-C_3N_4/Fe_2O_3 hybrids were studied. Detail characterizations on charge transfer kinetics revealed that g-C_3N_4/nanodot-Fe_2O_3 structure showed faster electron injection rate and higher injection efficiency ($\approx$0.084 ns^{-1} and $\approx$27.5%) than g-C_3N_4/nanosheet-Fe_2O_3 counterpart ($\approx$0.054 ns^{-1} and $\approx$19.5%). Stronger intimate junction between g-C_3N_4 nanosheets and Fe_2O_3 nanodots was believed to be the reason for faster and more efficient electron injection. In addition, stronger interaction with tetracycline and higher reactivity with H_2O_2 at the interface were observed for g-C_3N_4/nanodot-Fe_2O_3 compared with g-C_3N_4/nanosheet-Fe_2O_3. Thereby, under visible light stimulation, g-C_3N_4/nanodot-Fe_2O_3 demonstrated higher photo-Fenton-like tetracycline removal efficiency and rate ($\approx$87% and $\approx$0.037 min^{-1}) than g-C_3N_4/nanosheet-Fe_2O_3 ($\approx$57% and $\approx$0.016 min^{-1}). Furthermore, g-C_3N_4/nanodot-Fe_2O_3 junction can remain robust catalytic performance under various conditions (recycle experiment, real environment, different initial pHs and temperatures, anion coexistence, and other contaminants removal) and possible tetracycline degradation pathways were proposed. This study provided deep insights into structure-activity relationship and electron transfer between g-C_3N_4 and nanostructured Fe_2O_3, which can open a new avenge to develop Fe_2O_3-based photo-Fenton catalysts with high efficiencies for antibiotic wastewaters remediation.

Funding resources

1. National Natural Science Foundation of China (No. 21806059).
2. Natural Science Foundation of Jiangsu Higher Education Institution (No. 17KJB610006).
3. China Postdoctoral Science Foundation (No. 2018M630524).
4. Hong Kong Scholars Program of Society of Hong Kong Scholars (No. XJ2018031).
5. Research Grant Council, University Grants Council (No. GRF14100115) and Technology and Business Development Fund, The Chinese University of Hong Kong (No. TBF18SCI006).

1. Introduction

Antibictics such as tetracyclines (TCs) have been proverbially employed to treat baterial and protozoan infections in aquaculture (Chen et al., 2017), leading to the occurrence of different residues in ecosystems, for example, the soils and surface water have the concentration of being as high as $\approx$86–199 μg kg^{-1} and $\approx$0.13–0.51 μg L^{-1}, respectively (Wang et al., 2016; Yan et al., 2017). Due to the potential threat to ecological environment and human health even at a very low concentration, such as the perturbations in ecosystems, antibiotic resistance to bacteria, and possible risks to human health via the food chain (Trovo et al., 2011; Xue et al., 2015), a widespread attention has been paid for the development of effective materials and/or methods for

---

[*] Corresponding author.
[**] Corresponding author. School of Life Sciences, The Chinese University of Hong Kong, Shatin, NT, Hong Kong SAR, China.
E-mail addresses: yangshijiangsq@163.com (S. Yang), pkwong@cuhk.edu.hk (P.K. Wong).

https://doi.org/10.1016/j.envres.2021.110842
Received 1 November 2020; Received in revised form 24 January 2021; Accepted 31 January 2021

the elimination of antibiotic contaminations from environmental waters.

Advanced oxidation processes (AOPs) have been widely applied to remove emerging contaminants from aquatic environments (Andreozzi et al., 1999; Miklos et al., 2018). As one of the popular AOPs, the photo-Fenton reaction in which hydroxyl radicals (•OH) are generated from light radiation and hydrogen peroxide (H_2O_2) in the presence of iron-containing substances is highly recognized for the important advantages of being effective in removing various contaminants, working under simple conditions and the low price of the oxidation reagents (Clarizia et al., 2017; Herney-Ramireza et al., 2010; Pouran et al., 2015). Futhermore, the possibility of utilizing solar energy in the photo-Fenton process helps improving the economic and environmental sustainability. Nevertheless, the photo-Fenton system based on homogeneous iron salt-based catalysts usually has three obvious shortcomings: (i) The strict acidic medium (optimized pH 2.8–3.5) must be employed that not only restricts the application but also corrodes the equipment; (ii) A lot of iron-containing sludges are generated which induces an adverse impact on the environment and waste disposal problems; And (iii) a large amount of catalytic metals are misplaced in the sludge and regeneration of the catalyst is impracticable. All these issues strongly suggest the application of heterogeneous catalysis as alternative (Herney-Ramireza et al., 2010; Pouran et al., 2015). As a result, in the past years, the exploitation of effective heterogeneous catalysts has attracted a great deal of interest.

Recently, coupling solid iron-based Fenton catalysts with semiconductor photocatalysts has been extensively studied which has been proven to be a promising heterogeneous catalytic material with efficient photo-Fenton activity (Du et al., 2017; Guo et al., 2019a,b; Lima et al., 2017; Yang et al., 2015; Zhao et al., 2020). In such configuration, the photogenerated electrons from photocatalysts can inject to $\equiv Fe^{3+}$ to promote the regeneration of $\equiv Fe^{2+}$ on the surface, leading to the accelerated transformation from H_2O_2 to •OH radicals. In addition, the distributions of Fenton catalysts tend to be improved, thus more active sites are exposed that facilitates the interaction with H_2O_2 and pollutants. Owing to the instinctive features of environmental friendliness, low cost, corrosion-resistance, thermodynamic stability and non-toxicity (Zhu et al., 2013; Jiang et al., 2018), Fe_2O_3 is regarded as an attractive Fenton catalyst to hybridize various photocatalysts. For instance, Su et al. (2015) reported the synthesis of Fe_2O_3 incorporated TiO_2 nanotube arrays junction and observed its enhanced catalytic activity toward acid orange II degradation in the presence of H_2O_2 under UV irradiation. Xi et al. (2019) developed the 0D/2D hybrid of Fe_2O_3/g-C_3N_4 that was employed as an effective catalyst for the elimination of p-nitrophenol in the photo-Fenton-like process. Zhang et al. (2017) fabricated the three-dimensionally ordered microporous $BiVO_4$ supported Fe_2O_3 heterostructure which showed excellent photo-Fenton-like performance for p-nitrophenol removal. Nevertheless, little is known about the fundamental morphological effect and charge transfer behavior between photocatalysts and Fe_2O_3 Fenton catalysts with different shapes, structures and deposition strategies, which plays a crucial role in explaining and promoting photo-Fenton-like activity. Furthermore, these basic studies on structure-activity relationship and photophysical property also provide important guidance for the design and synthesis of effective heterogeneous catalysts in the photo-Fenton system.

Therefore, in this study, having multiple virtues of abundant composition, easy availability, robust structure and eco-friendliness (Fu et al., 2017; Jiang et al., 2020; Ong et al., 2016; Wang et al., 2020a,b), g-C_3N_4 nanosheets were used as representative photocatalysts to support two different morphologies of Fe_2O_3 including nanodots and nanosheets, which were synthesized by *in-situ* deposition and impregnation-hydrothermal methods, respectively. It was found that the photo-Fenton-like activity of g-C_3N_4 toward TC degradation was greatly enhanced after modification with Fe_2O_3 nanodots, that was much higher than Fe_2O_3 nanosheets decorated g-C_3N_4. The electron transfer dynamics, injection rate and injection efficiency of these two g-C_3N_4/Fe_2O_3 junctions were explored. Appropriate mechanisms were proposed to elucidate their difference in catalytic activity. In addition, the photo-Fenton-like stability of Fe_2O_3 nanodots modified g-C_3N_4 was investigated. Meanwhile, possible TC degradation pathways were discussed. This study would provide a new strategy by designing optimized Fenton catalyst structures and loading methods to construct effective heterogeneous photo-Fenton catalysts for the remediation of antibictic wastewaters.

2. Materials and methods

2.1. Chemicals

Tetracycline, rhodamine B and phenol are purchased from Aladdin (China). Ammonium oxalate, *tert*-butanol, hydrogen peroxide (30 wt%), sodium hydroxide, hydrochloric acid (36–38 wt%), terephthalic acid are purchased from Sinopharm (China). Urea, ferric chloride, ferric nitrate, ammonium bicarbonate, sodium acetate, sodium sulfate, isopropanol, nafion solution (5 wt%) are purchased from Sigma-Aldrich (USA). All the chemicals are analytic reagents.

2.2. Materials preparation

2.2.1. Synthesis of g-C_3N_4

The g-C_3N_4 nanosheets were synthesized through a thermal polymerization-etching strategy. In short, approximately 30 g of urea was added into a covered crucible and heated to 550 °C for 4 h. The obtained yellow substance with mass of 400 mg was further heated to 500 °C for 2 h in an open crucible. The resultant light-yellow product was g-C_3N_4 nanosheets. It was noted that a covered crucible should be used in the first step of thermal treatment to prevent volatilization of intermediates in the thermal polymerization of urea at a high temperature to generate g-C_3N_4. In addition, an uncovered crucible was utilized in the second stage to make g-C_3N_4 be exfoliated to nanosheet morphology in air via a thermal oxidation etching.

2.2.2. Synthesis of g-C_3N_4/ND-Fe_2O_3 hybrid

The synthesis of g-C_3N_4/4.0%ND-Fe_2O_3 was based on an *in-situ* deposition method. In a typical synthesis, g-C_3N_4 nanosheets with mass of 200 mg were dispersed in 100 mL of ethanol. Then, 0.1 mmol of ferric nitrate was dissolved in the prepared g-C_3N_4 suspension. After this, 3.0 mmol of ammonium bicarbonate was added, and the reaction system was kept continuous stirring. After the reaction of 10 h, the obtained product was collected by centrifugation, washed with ethanol several times, dried at 60 °C in a vacuum oven, and annealed at 350 °C for 2 h in air. The resultant product was g-C_3N_4/4.0%ND-Fe_2O_3 composite in which 4.0% represented the theoretical weight percentage of Fe_2O_3 NDs loading. When g-C_3N_4 nanosheets were not presented in the preparation procedure, pure Fe_2O_3 NDs with size of 3–5 nm would be acquired (Fig. S1). In addition, the g-C_3N_4/2.0%ND-Fe_2O_3 and g-C_3N_4/8.0%ND-Fe_2O_3 counterparts were prepared under this synthesis condition through changing the addition amount of g-C_3N_4 nanosheets as 400 and 100 mg, respectively.

2.2.3. Synthesis of g-C_3N_4/NS-Fe_2O_3 hybrid

Fe_2O_3 NSs should be first synthesized via a reported hydrothermal method (Chen et al., 2010). Typically, 0.68 g of ferric chloride was added into the mixture of water (1.75 mL) and ethanol (25 mL) with agitation. After dissolution of ferric chloride, 2.0 g of sodium acetate was added. The obtained dispersion was then transferred to a Teflon-lined stainless-steel autoclave (50 mL) and maintained at 180 °C for 12 h. The obtained red product was Fe_2O_3 NSs which should be collected by centrifugation, washed with water and ethanol, and dried at 60 °C under a vacuum condition. Secondly, an impregnation-hydrothermal strategy was used to synthesize g-C_3N_4/4.0%NS-Fe_2O_3 hybrid. In a typical synthesis, 100 mg of g-C_3N_4 nanosheets were added to 50 mL of ethanol solution and ultrasonicated for 30 min. 4.0 mg of Fe_2O_3 NSs was then dispersed into g-C_3N_4 suspension and stirred for 6 h. The obtained dispersion was transferred to a Teflon-lined stainless-steel autoclave (100 mL) and heated at 150 °C for 4 h. After collection and drying, the g-C_3N_4/4.0%NS-Fe_2O_3 product was acquired where 4.0% likewise referred to the theoretical weight percentage of loaded Fe_2O_3 NSs. For comparison, the g-C_3N_4/1.0%NS-Fe_2O_3 and g-C_3N_4/8.0%NS-Fe_2O_3 composites were synthesized under this condition via varying the addition mass of Fe_2O_3 NSs as 1.0 and 8.0 mg, respectively.

2.3. Characterization

Powder X-ray diffraction (XRD) patterns of samples were acquired using the Bruker AXS D8 ADVANCE X-ray diffractometer with Cu Kα radiation ($\lambda = 0.154178$ nm). X-ray photoelectron spectroscopy (XPS) was conducted using the Thermo ESCALAB 250 Xi spectrometer with the monochromatized Al Kα source. Transmission electron microscopy (TEM), high-resolution TEM, high angle annular dark field scanning transmission electron microscopy (HAADF-STEM), and energy dispersive X-ray (EDX) spectroscopy were performed using the FEI-Tecnai G2 F20 microscope. Fourier transform infrared (FTIR) spectra were characterized by the Nicolet 6700 spectrometer. UV–vis diffuse reflection spectra were obtained using the Macy UV-1800APC spectrometer with the reference of barium sulfate. The content of iron in the sample is measured by using PERSEE A3 atomic absorption spectrophotometer. Photoluminescence (PL) and time-resolved fluorescence decay (TRFD) measurements were performed using the Edinburgh FLS980 fluorescence spectrometer. Electrochemical impedance spectroscopy (EIS) spectra and transient photocurrent (TPC) curves were recorded using the CHI 650E electrochemical workstation equipped with a standard three-electrode cell including a working electrode, a reference electrode (Ag/AgCl) and a counter electrode (Pt plate). 0.5 M sodium sulfate solution and 300 W Xenon lamp (visible light) were used as the electrolyte and light source, respectively. A dip-coating method was utilized to prepare the working electrode: (i) The sample (5 mg) was added into a mixed solution of nafion (20 μL) and isopropanol (1 mL); (ii) The obtained suspension was homogeneously dispersed by sonication; And (iii) the resultant dispersion was dip-coated on the 1×1 cm^2 FTO glass which was then dried in a fume hood overnight to obtain the working electrode. The fluorescence spectra were recorded using a Varian Cary Eclipse spectrometer at the excitation wavelength of 310 nm. Prior to experiment, the terephthalic acid solution with a concentration of 0.75 mM should be first prepared via dissolving terephthalic acid into 2 mM sodium hydroxide solution; Then, 20 mg of catalyst was dispersed into 100 mL of terephthalic acid solution for detection. The degradation products of TC are determined by liquid chromatography-mass spectrometry (LC-MS) performed on a Waters SYNAPT MS system.

2.4. Activity assessment

In a typical TC degradation, a catalyst with mass of 20 mg was dispersed into 100 mL of 20 mg L^{-1} TC aqueous solution. The degradation experiment was initiated at 25 °C by the addition of H_2O_2 and simultaneously turning on visible light (300 W Xenon lamp, Perfect-Light). The H_2O_2 concentration and light intensity were controlled to be 50 mM and 2500 W m^{-2}, respectively. Before initiation, the reaction solution needed to be stirred for 30 min in dark to establish the adsorption equilibrium. At certain time intervals, aliquots with volume of 2.5 mL were extracted and filtered by 0.22 μm microporous membrane. The TC concentration in the filtrate was determined using a UV–vis spectrophotometer at the maximum absorption wavelength of 357 nm. TC degradation efficiency was determined by the following formula:

$$\text{Efficiency of TC degradation}(\%) = (C_0 - C)/C_0 \times 100$$

where C_0 (mg L^{-1}) and C (mg L^{-1}) were the initial and final TC concentration, respectively. For comparison, the blank TC degradation without adding catalyst in the presence of H_2O_2 under visible light irradiation was determined. Furthermore, in the experiment to evaluate the effect of leaching iron species, 20 mg of catalyst was first dispersed into 100 mL of water and stirred for several hours in dark. Then, the solid catalyst should be removed by filtration and the acquired filtrate was the reaction solution containing potential leaching iron species. After that, TC pollutant was added with a concentration of 20 mg L^{-1} and the degradation experiment was performed after addition of 50 mM H_2O_2 under visible light irradiation.

TC adsorption was carried out under the same condition as degradation but in the absence of H_2O_2 and light irradiation. In the recycle experiment, the catalyst after one run should be collected by centrifugation and washed by ethanol for the next run. The initial pH of reaction solution was adjusted by hydrochloric acid and sodium hydroxide solution. The corresponding sodium salts with a typical concentration of 1.0 mM were used as the sources for different coexisting anions in the catalytic process. In the catalytic removal of rhodamine B and phenol pollutants, the similar colorimetric method at the maximum absorption wavelength of 553 nm was applied to detect rhodamine B. For the determination of phenol, the high-performance liquid chromatography equipped with a reversed C18-column and UV detector was utilized. The adsorption wavelength was set to be 270 nm. The mobile phase was a mixture of water (30 vol%) and methanol (70 vol%). In order to determine reactive species for TC degradation, ammonium oxalate (10 mM), *tert*-butanol (50 mM), and nitrogen gas (50–100 mL min^{-1}) needed to be added respectively to quench the probably generated holes, •OH and $\bullet O_2^-$ radicals in the reaction system.

3. Results and discussion

The formations of g-C_3N_4/ND-Fe_2O_3 and g-C_3N_4/ND-Fe_2O_3 were analyzed. For g-C_3N_4/ND-Fe_2O_3, its formation mechanism can be summarized as: The average zeta potential of g-C_3N_4 nanosheets was −26.4 mV (Fig. S2), the added Fe^{3+} ions were easily adsorbed on their surface via electro-static interaction (Gao et al., 2018). Generally, the N atoms in g-C_3N_4 networks were reported as primary complex sites to connect metal ions (Gao et al., 2018). Therefore, the agglomeration of Fe^{3+} ions was significantly prohibited. When NH_4HCO_3 substance was introduced, these anchored Fe^{3+} ions can react with it and amorphous FeOOH NDs were *in-situ* formed (Liu et al., 2016), as seen from its TEM image (Fig. S3). These FeOOH species were decomposed into Fe_2O_3 after calcination. Since the confinement effect of g-C_3N_4 frameworks can effectively hinder the overgrowth of amorphous nanoparticles (Wang et al., 2014; Ye et al., 2017), Fe_2O_3 NDs were generated on g-C_3N_4 nanosheets with good distribution. Meanwhile, heat treatment also can strengthen the bond between g-C_3N_4 and Fe_2O_3 NDs. Regarding the synthesis of g-C_3N_4/NS-Fe_2O_3 hybrid, firstly, the dispersed Fe_2O_3 NSs were physically deposited onto g-C_3N_4 nanosheets. Then, the connection between them was enhanced by high temperature and high pressure hydrothermal treatment. Table S1 summarized the real contents of Fe_2O_3 components which were consistent with its theoretical value, further indicating the synthesis of these g-C_3N_4/Fe_2O_3 hybrids.

Texture and optical properties of g-C_3N_4/4.0%ND-Fe_2O_3 and g-C_3N_4/4.0%NS-Fe_2O_3 were characterized by XRD patterns, FTIR spectra and UV–vis diffuse diffraction spectra. As shown in the XRD patterns (Fig. 1a), similar to pristine g-C_3N_4, g-C_3N_4/4.0%ND-Fe_2O_3 and g-C_3N_4/4.0%NS-Fe_2O_3 hybrids clearly displayed the feature (100) and (002) diffraction peaks at ≈12.7° and ≈27.4° relating to the in-plane structural repeating motifs of the aromatic systems and the interlayer reflections of the graphitic-like structures (Han et al., 2015; Zhang et al., 2012), demonstrating that the loadings of Fe_2O_3 (NDs and NSs) did not alter the crystalline structure of g-C_3N_4. Owing to the surface modification with Fe_2O_3, several distinct diffraction peaks at ≈24.1°, ≈33.1°, ≈35.6°, ≈40.8°, ≈49.4°, ≈54.0°, ≈62.4° and ≈64.0° individually

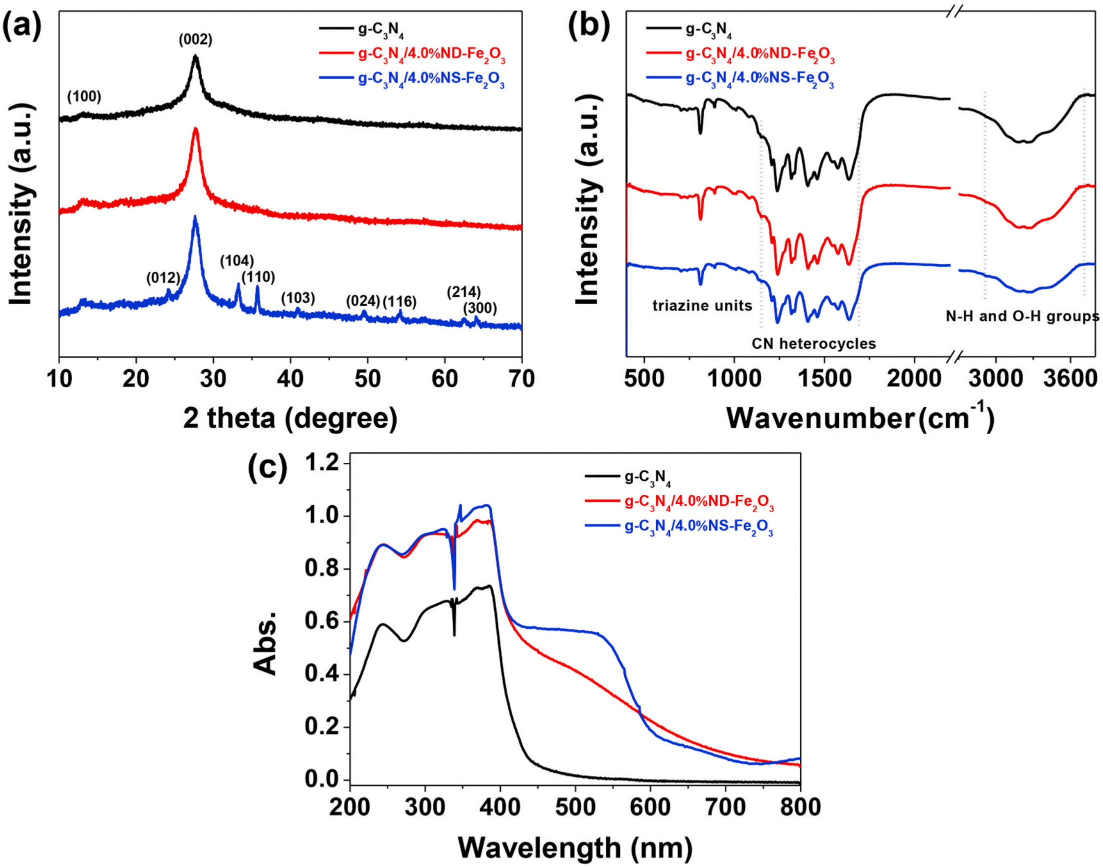

Fig. 1. XRD patterns (a), FTIR spectra (b) and UV–vis diffuse reflection spectra (c) of g-C_3N_4, g-C_3N_4/4.0%ND-Fe_2O_3 and g-C_3N_4/4.0%NS-Fe_2O_3.

corresponding to (012), (104), (110), (113), (024), (116), (214) and (300) planes of α-Fe_2O_3 in Fe_2O_3 NSs (Fig. S3) were observed for g-C_3N_4/4.0%NS-Fe_2O_3. However, no obvious characteristic evidence attributed to α-Fe_2O_3 in Fe_2O_3 NDs (Fig. S4) was sought for g-C_3N_4/4.0% ND-Fe_2O_3, even in the case of g-C_3N_4/8.0%ND-Fe_2O_3 (Fig. S4), which was presumbely due to the small size and homogeneous distribution of Fe_2O_3 NDs onto g-C_3N_4 nanosheets (Zhao et al., 2021). In the FTIR spectra (Fig. 1b), g-C_3N_4/4.0%ND-Fe_2O_3 and g-C_3N_4/4.0%NS-Fe_2O_3 heterojunctions nearly exhibited the unaltered absorption bands with g-C_3N_4, which further illustrated that both Fe_2O_3 NDs and Fe_2O_3 NSs loadings hardly varied the chemical structure of g-C_3N_4, well consistent with XRD patterns. Typically, the pronouced absorption peaks at ≈1209, ≈1240, ≈1317, ≈1408, ≈1460, ≈1575 and ≈1636 cm^{-1} were ascribed to the stretching vibration of CN heterocycles; The appeared sharp peak at ≈812 cm^{-1} was related to the breathing vibration of triazine untis; And the wide band in 2800–3700 cm^{-1} corresponded to the residual N–H and O–H functions which were connected with uncondensed amino groups and surface-adsorbed water molecules (Han et al., 2015; Zhang et al., 2012). Probably because of the low loading content, no obvious FTIR diffraction peak ascribed to Fe_2O_3 (Fig. S5) was evidenced in these two composites. From the UV–vis diffuse reflection spectra (Fig. 1c), g-C_3N_4 showed an absorption edge at about 440 nm that was in good accordance with the reported absorption of its nanosheet morphology (Liu et al., 2019; Xu et al., 2017). As expected, the obviously improved visile-light absorptions were found for g-C_3N_4/4.0%ND-Fe_2O_3 and g-C_3N_4/4.0%NS-Fe_2O_3 heterostructures, presumbly resulting from the increased backgroud absorptions of Fe_2O_3 NDs and Fe_2O_3 NSs in the visible region (Fig. S6). In addition, it was noticed that the absorption edge of g-C_3N_4 seemed to be shifted to higher wavelength when Fe_2O_3 (NDs and NSs) was loaded, which was the result of the interaction at the interface (Ge et al., 2012).

The morphologies and microstructures of g-C_3N_4/4.0%ND-Fe_2O_3 and g-C_3N_4/4.0%NS-Fe_2O_3 were studied by TEM technique. As seen from the low-magnification TEM image of g-C_3N_4/4.0%ND-Fe_2O_3 hybrid (Fig. 1a), the hierarchical morphology with interconnected nanosheets was clearly presented which was the same as pristine g-C_3N_4 (Fig. S7), indicating that the modification with Fe_2O_3 NDs did not change the morphology of g-C_3N_4. Nearly no Fe_2O_3 NDs was found to be deposited onto g-C_3N_4 perhaps owing to the small size. In the high-magnification TEM images (Fig. 1b and c), it was apparently observed that Fe_2O_3 NDs with the size of around 3–5 nm were homogeneously dispersed onto g-C_3N_4, which can be further confirmed by the HAADF-STEM images (Fig. S8). The lattice spacing of ≈0.25 nm in the high-resolution TEM image (Fig. 1d) corresponded to (110) plane of α-Fe_2O_3. Based on the HAADF-STEM-EDX elemental mapping images (Fig. 1e), the presence of C, N, O and Fe elements were unambiguously confirmed as well as the O and Fe elements were uniformly dispersed, further confirming the homogenous distribution of Fe_2O_3 NDs. For g-C_3N_4/4.0%NS-Fe_2O_3 composite, the same hierarchical structure comprised of crumpled nanosheets was observed in the low-magnification TEM image (Fig. 1f), meaning that the introduction of Fe_2O_3 NSs also did not alter the shape of g-C_3N_4. At the same time, the Fe_2O_3 species was obviously discovered. From the high-magnification TEM images (Fig. 1g and h), the deposited Fe_2O_3 showed a morphology of hexagonal nanosheets with a width of ≈200 nm and a thickness of ≈10 nm. Moreover, we noted that these nanosheets were prone to aggregate together that was presumbly ascribed to the weak coupling with g-C_3N_4. The lattice spacing of ≈0.25 nm corresponding to (110) plane of α-Fe_2O_3 was also measured in the high-resolution TEM image (Fig. 1i). The HAADF-STEM-EDX elemental mapping images (Fig. 1j) also indicated that Fe_2O_3 nanosheets were decorated on the surface of g-C_3N_4.

The XPS measurements were performed to investigate the surface chemical states of g-C_3N_4/4.0%ND-Fe_2O_3 and g-C_3N_4/4.0%NS-Fe_2O_3. In the high C1s spectrum (Fig. 3a), g-C_3N_4/4.0%ND-Fe_2O_3 exhibited two deconvolution peaks at ≈288.4 and ≈284. 8 eV while these two peaks apppeared at ≈288.1 and ≈284. 8 eV in g-C_3N_4/4.0%NS-Fe_2O_3, which corresponded to the sp^2 C–C bonds and sp^2 hybridized carbon in N-containing aromatic rings (N–C═N), respectively (Han et al., 2015; Zhang et al., 2012). Compared with pristine g-C_3N_4, the typical peak allying with sp^2 hybridized carbon in g-C_3N_4/4.0%ND-Fe_2O_3 shifted to higher binding energy by ≈0.3 eV while g-C_3N_4/4.0%NS-Fe_2O_3 almost showed no obvious shift. As presented in Fig. 2b, the high-resolution N 1s spectra of both g-C_3N_4/4.0%ND-Fe_2O_3 and g-C_3N_4/4.0%NS-Fe_2O_3 displayed three deconvolution peaks at ≈401.1 and ≈400.9 eV, ≈399.8 and ≈399.6 eV, as well as ≈398.8 and ≈398.6 eV, which were correlated with the amino functions (C–N–H), tertiary nitrogen N-$(C)_3$ groups and sp^2 hybridized nitrogen involved in triazine rings (C–N═C), respectively (Han et al., 2015; Zhang et al., 2012). In contrast to pristine g-C_3N_4, we noted that these characteristic nitrogen peaks in g-C_3N_4/4.0%ND-Fe_2O_3 shifted to higher binding energy by ≈0.3 eV while the smaller shift by ≈0.1 eV was determined for g-C_3N_4/4.0%NS-Fe_2O_3. From the high-resolution Fe 2p spectra (Fig. 3c), it was observed that g-C_3N_4/4.0%ND-Fe_2O_3 displayed two major peaks at ≈710.5 and ≈723.9 eV which were attributed to Fe 2p3/2 and Fe 2p1/2 of Fe_2O_3, respectively (Guo et al., 2019a,b; Li et al., 2017a,b). Different from the changes of C 1s and N 1s spectra, these two peaks were found to shift to lower binding energy by ≈0.3 eV when compared with Fe_2O_3 NDs. Likewise, the feature peaks at ≈710.7 and ≈724.1 eV relating to Fe_2O_3 in g-C_3N_4/4.0%ND-Fe_2O_3 shifted to lower binding energies by ≈0.2 eV in comparison with Fe_2O_3 NSs. Furthermore, it can be seen from Fig. 3d that there were two deconvolution peaks emerged at ≈529.4 and ≈532.1 eV in the high-resolution O 1s spectrum of g-C_3N_4/4.0% ND-Fe_2O_3 that were ascribed to the lattice oxygen of Fe_2O_3 and surface-adsorbed water molecules, respectively (Guo et al., 2019a,b; Li et al., 2017a,b). While Fe_2O_3 NDs showed the same two deconvolution peaks at ≈529.6 and ≈531.2 eV which were linked with the lattice oxygen of Fe_2O_3 and hydroxyls adsorbed on the surface, respectively (Guo et al., 2019a,b; Li et al., 2017a,b). In agreement with the variation of Fe 2p, the representative lattice oxygen-related peak in g-C_3N_4/4.0%

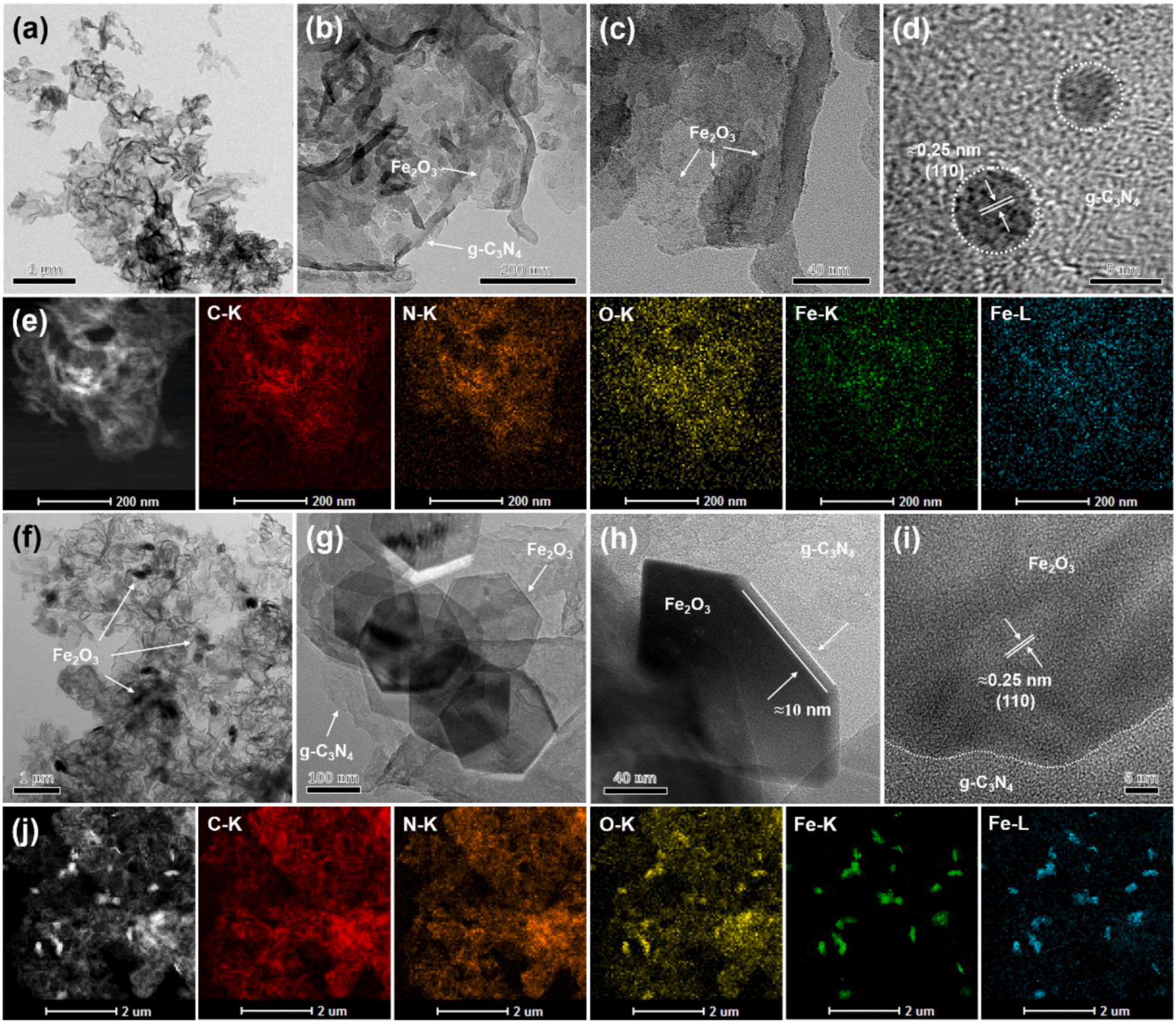

Fig. 2. Low-magnification TEM (a), high-magnification TEM (b, c), high-resolution TEM (d) and HAADF-STEM-EDX elemental mapping (e) images of g-C_3N_4/4.0% ND-Fe_2O_3; Low-magnification TEM (f), high-magnification TEM (g, h), high-resolution TEM (i) and HAADF-STEM-EDX elemental mapping (j) images of g-C_3N_4/4.0% NS-Fe_2O_3.

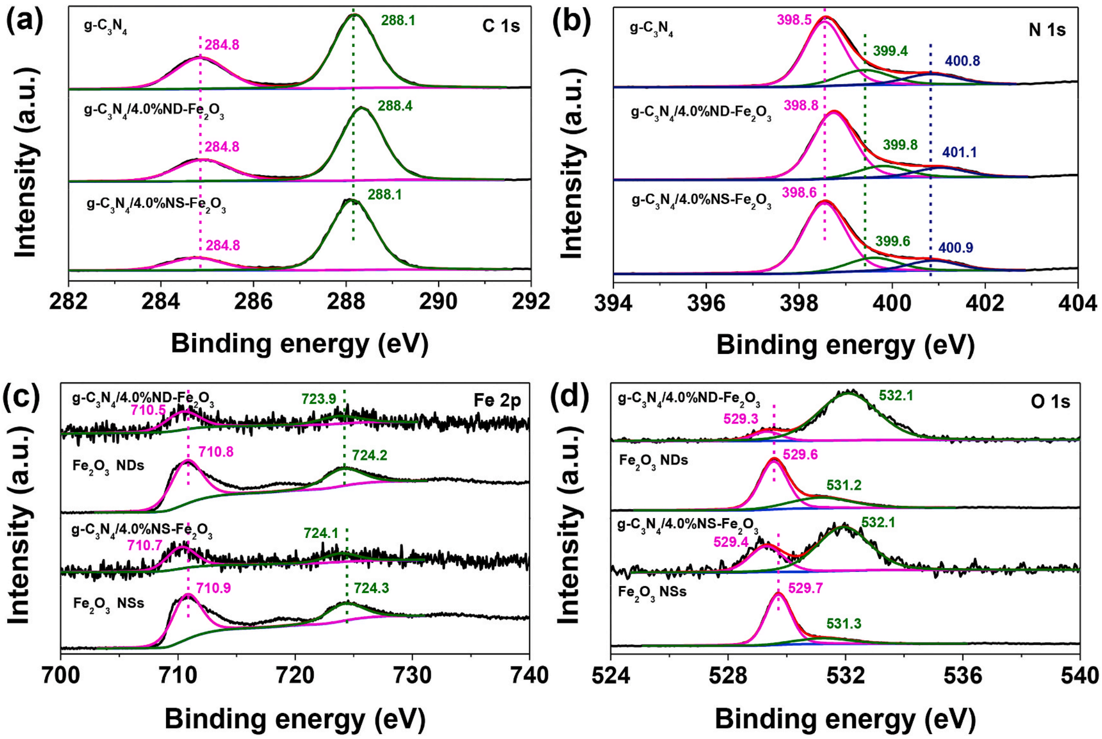

Fig. 3. High-resolution XPS spectra of C 1s (a), N 1s (b), Fe 2p (c) and O 1s (d) in g-C_3N_4, g-C_3N_4/4.0%ND-Fe_2O_3, g-C_3N_4/4.0%NS-Fe_2O_3, Fe_2O_3 NDs and Fe_2O_3 NSs.

ND-Fe_2O_3 shifted to lower binding energy by ≈0.3 eV compared with Fe_2O_3 NDs. Similarly, the peak associated with lattice oxygen in g-C_3N_4/4.0%NS-Fe_2O_3 was ≈0.3 eV lower than that in Fe_2O_3 NSs. In other words, these results indicated that the binding energies of C 1s and N 1s in g-C_3N_4/4.0%ND-Fe_2O_3 and g-C_3N_4/4.0%NS-Fe_2O_3 were higher than those in g-C_3N_4, while the binding energies of Fe 2p and O 1s were lower than those in Fe_2O_3 NDs and Fe_2O_3 NSs. According to the previous studies, these binding energy shifts can be attributed to the electronic interaction between g-C_3N_4 and Fe_2O_3 (Jiang et al., 2015; Zhang et al., 2015). In general, g-C_3N_4/4.0%ND-Fe_2O_3 manifested the larger shift than g-C_3N_4/4.0%NS-Fe_2O_3 based on the XPS analysis. As a result, a stronger interaction between Fe_2O_3 NDs and g-C_3N_4 was achieved at the interface.

The photo-Fenton-like activities of samples were examined by TC degradation in the presence of H_2O_2 under visible light stimulation. As displayed in Fig. 4a, just ≈10% of TC molecules were degraded within the reaction time of 60 min in the blank experiment. When g-C_3N_4/4.0% ND-Fe_2O_3 and g-C_3N_4/4.0%NS-Fe_2O_3 were presented in the system, both the TC degradations were significantly increased, indicating their efficient photo-Fenton-like activities. In contrast, the slower TC degradation was observed for g-C_3N_4 under the same condition. Accordingly, we believed that the improved activities over g-C_3N_4/4.0%ND-Fe_2O_3 and g-C_3N_4/4.0%NS-Fe_2O_3 resulted from the synergistic effect between g-C_3N_4 and Fe_2O_3 (NDs and NSs). The measured TC degradation efficiency of g-C_3N_4/4.0%ND-Fe_2O_3 was ≈87% while ≈57% for g-C_3N_4/4.0%NS-Fe_2O_3 that was much lower. To evaluate the effect of possible leached iron, the content of leached iron in the solution was measured. The g-C_3N_4/4.0%ND-Fe_2O_3 composite exhibited a low iron leaching concentration of ≈0.15 μg/mL in the reaction process and nearly no iron leaching was determined for g-C_3N_4/4.0%NS-Fe_2O_3. Furthermore, together with much lower contribution to TC degradation from leached iron (Fig. S9), the heterogeneous photo-Fenton-like process was regarded as main reactive approach for TC degradation in the presence of g-C_3N_4/4.0%ND-Fe_2O_3 and g-C_3N_4/4.0%NS-Fe_2O_3. Compared with pure

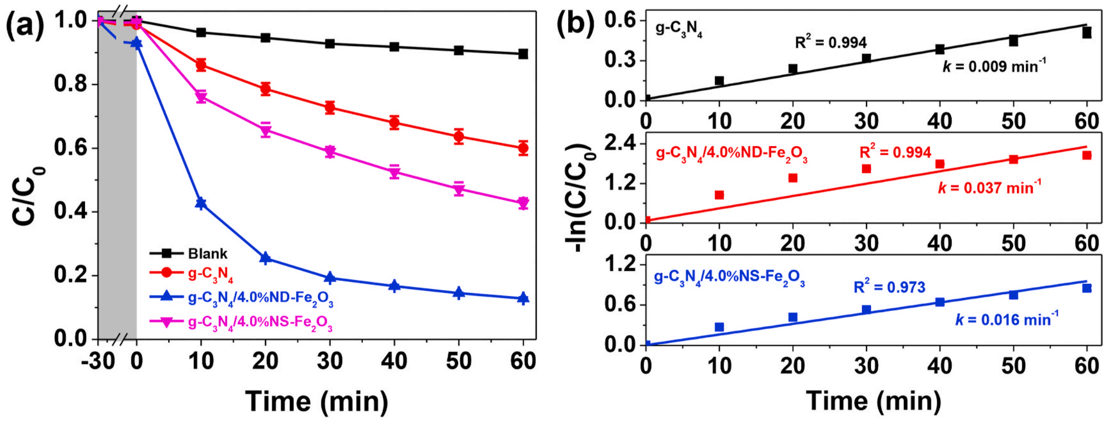

Fig. 4. TC degradation activities (a) and kinetics (b) over g-C_3N_4, g-C_3N_4/4.0%ND-Fe_2O_3 and g-C_3N_4/4.0%NS-Fe_2O_3 in the presence of H_2O_2 under visible light irradiation.

photocatalytic and Fenton-like TC degradation (Fig. S10), the efficient photo-Fenton-like activity of g-C_3N_4/4.0%ND-Fe_2O_3 was a synergistic result between photocatalysis and Fenton-like action. In addition, the TC degradation kinetics were studied, as displayed in Fig. 4b. Evidently, all the TC degradations over g-C_3N_4, g-C_3N_4/4.0%ND-Fe_2O_3 and g-C_3N_4/4.0%NS-Fe_2O_3 followed the pseudo-first-order kinetics equation:

$$-\ln(C/C_0) = kt \tag{2}$$

where t (min) was the reaction time, k (min^{-1}) was the apparent rate constant, and C_0 (mg L^{-1}) and C (mg L^{-1}) were the initial and final TC concentrations, respectively. As expected, g-C_3N_4/4.0%ND-Fe_2O_3 showed the higher first-order rate constant of ≈0.037 min^{-1} than that for g-C_3N_4 (≈0.009 min^{-1}) and g-C_3N_4/4.0%NS-Fe_2O_3 (≈0.016 min^{-1}). All of these results well illustrated that the prepared Fe_2O_3 NDs decorated g-C_3N_4 junction possessed the more efficient photo-Fenton-like performance toward TC removal than the Fe_2O_3 NSs-modified g-C_3N_4 counterpart. Moreover, as seen from Fig. S11, g-C_3N_4/4.0%ND-Fe_2O_3 also exhibited higher TC degradation efficiency and rate than common iron-based counterparts, further demonstrating the efficient photo-Fenton-like activity. The loading amount of Fe_2O_3 NDs and Fe_2O_3 NSs was found to affect the photo-Fenton-like activity of g-C_3N_4/ND-Fe_2O_3 and g-C_3N_4/NS-Fe_2O_3, respectively. As shown in Fig. S12a, as the content of Fe_2O_3 NDs increased to 4.0 wt%, the peak TC degradation was obtained for g-C_3N_4/ND-Fe_2O_3. Unfortunately, further increasing their content to 8.0 wt% produced a slightly declined performance. For g-C_3N_4/NS-Fe_2O_3 (Fig. S12b), an obvious enhancement of TC removal was observed when the content of Fe_2O_3 NSs increased from 1.0 to 4.0 wt%. However, this improvement become much slower when the loading content of Fe_2O_3 NSs further increased to 8.0 wt%. These results were presumbly because the overloaded Fe_2O_3 also acted as the recombination sites of photoinduced charge carriers and hindered the light absorption of g-C_3N_4 support as well (Ran et al., 2014).

The interfacial charge transfer properties between g-C_3N_4 and Fe_2O_3 (NDs and NSs) were studied by a set of photoelectrochemical measurements. As seen from the EIS spectra (Fig. 5a), the arc radiuses of g-C_3N_4/4.0%ND-Fe_2O_3 and g-C_3N_4/4.0%NS-Fe_2O_3 were smaller than that of g-C_3N_4, suggesting that the loading of Fe_2O_3 (NDs and NSs) reduced the charge transfer resistance of g-C_3N_4. Compared with g-C_3N_4/4.0%NS-Fe_2O_3, g-C_3N_4/4.0%ND-Fe_2O_3 displayed a lower charge transfer resistance in view of the smaller arc radius. These results demonstrated the easier separation of hole-electron pairs in g-C_3N_4/4.0%ND-Fe_2O_3. This conclusion was further verified by the TPC spectra (Fig. 5b). As shown, the photocurrent intensity followed a decreasing order of g-C_3N_4/4.0%ND-Fe_2O_3 > g-C_3N_4/4.0%NS-Fe_2O_3 > g-C_3N_4, illustrating that the separation and transfer of charge carriers in g-C_3N_4/4.0%ND-Fe_2O_3 was more efficient.

To further insight into the charge transfer mechanism between g-C_3N_4 and Fe_2O_3 (NDs and NSs), the PL and TRFD spectra of g-C_3N_4, g-C_3N_4/4.0%ND-Fe_2O_3 and g-C_3N_4/4.0%NS-Fe_2O_3 were recorded. According to the PL spectra (Fig. 6a), g-C_3N_4 showed the strongest peak intensity at ≈435 nm which was generally due to the fast recombination of hole-electron pairs. The obviously decreased PL intensities were determined for g-C_3N_4/4.0%ND-Fe_2O_3 and g-C_3N_4/4.0%NS-Fe_2O_3 hybrids, implying that the introduction of Fe_2O_3 (NDs and NSs) inhibited charge recombination and improved hole-electron separation. Contrast to g-C_3N_4/4.0%NS-Fe_2O_3, the lower PL intensity in g-C_3N_4/4.0%ND-Fe_2O_3 indicated that Fe_2O_3 NDs possessed higher charge separation efficiency. In the TRFD spectra (Fig. 6b), the fluorescence intensities of all samples decayed exponentially and the decay rate followed an order of g-C_3N_4/4.0%ND-Fe_2O_3 > g-C_3N_4/4.0%NS-Fe_2O_3 > g-C_3N_4. Fitting the decay spectra manifested three radiative lifetimes as summarized in Table 1 that were connected with the non-radiative process (τ_1), radiative process (τ_2) and energy transfer process (τ_3), respectively (Zhao et al., 2021). Clearly, the heterostructures of g-C_3N_4/4.0%ND-Fe_2O_3 ($\tau_1 = 0.55$, $\tau_2 = 2.00$ and $\tau_3 = 7.61$ ns) and g-C_3N_4/4.0%NS-Fe_2O_3 ($\tau_1 = 0.66$, $\tau_2 = 2.37$ and $\tau_3 = 8.79$ ns) displayed the shorter radiative lifetimes in contrast to g-C_3N_4 ($\tau_1 = 0.81$, $\tau_2 = 2.77$ and $\tau_3 = 9.55$ ns), representing that the photogenerated electrons from g-C_3N_4 were effectively trapped by Fe_2O_3 NDs and Fe_2O_3 NSs (Shi et al., 2018; Li et al., 2017a,b). Additionally, the lower radiative lifetime values in g-C_3N_4/4.0%ND-Fe_2O_3 contrast to g-C_3N_4/4.0%NS-Fe_2O_3 indicated the more efficient electron injection from g-C_3N_4 to Fe_2O_3 NDs. To directly observe electron transfer rate and efficiency from g-C_3N_4 to Fe_2O_3, the average radiative lifetime, τ_{ave}, was calculated according to the following equation (Zhen et al., 2018):

$$\tau_{ave} = \sum B_i\tau_i^2 \Big/ \sum B_i\tau_i \tag{3}$$

where B and τ referred to amplitudes and lifetimes, as given in Table 1. As expected, the average lifetime of g-C_3N_4/4.0%ND-Fe_2O_3 was ≈3.27 ns, which was shorter than that for g-C_3N_4/4.0%NS-Fe_2O_3 (≈3.63 ns) and g-C_3N_4 (≈4.51 ns), respectively (Table 1). This result also illustrated that the photoexcited electrons from g-C_3N_4 was rapidly injected to Fe_2O_3 NDs. On the basis of the average lifetimes of g-C_3N_4, g-C_3N_4/4.0% ND-Fe_2O_3 and g-C_3N_4/4.0%NS-Fe_2O_3, the injection rate of electron was determined using the following formula (Abdellah et al., 2013):

$$k_{ET} = 1/\tau_{ave}(g-C_3N_4/Fe_2O_3) - 1/\tau_{ave}(g-C_3N_4) \tag{4}$$

The measured k_{ET} value of g-C_3N_4/4.0%ND-Fe_2O_3 was ≈0.084 ns^{-1}, while ≈0.054 ns^{-1} for g-C_3N_4/4.0%NS-Fe_2O_3 which was much lower (Table 1). Moreover, the efficiency of electron injection (η_{inj}) from g-C_3N_4 to Fe_2O_3 was acquired via the following equation (Abdellah et al., 2013):

$$\eta_{inj} = 1 - \tau_{ave}(g-C_3N_4/Fe_2O_3)/\tau_{ave}(g-C_3N_4) \tag{5}$$

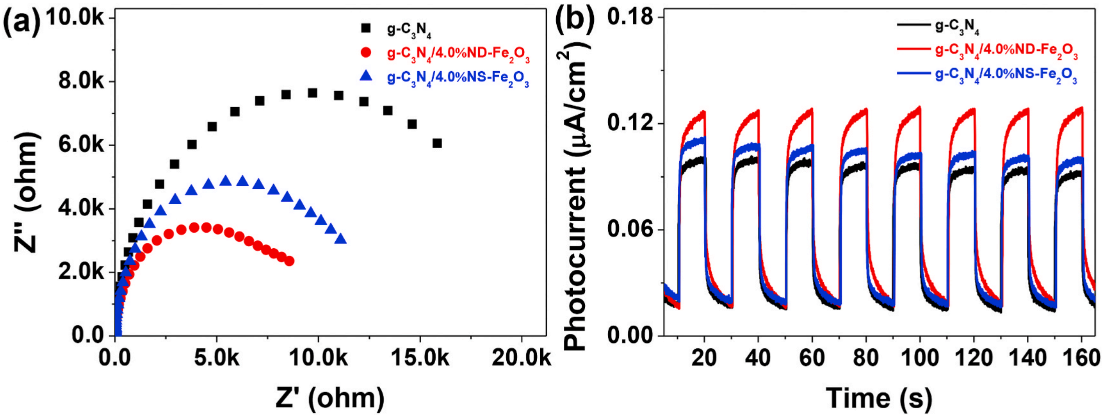

Fig. 5. EIS spectra (a) and TPC curves (b) of g-C_3N_4, g-C_3N_4/4.0%ND-Fe_2O_3 and g-C_3N_4/4.0%NS-Fe_2O_3.

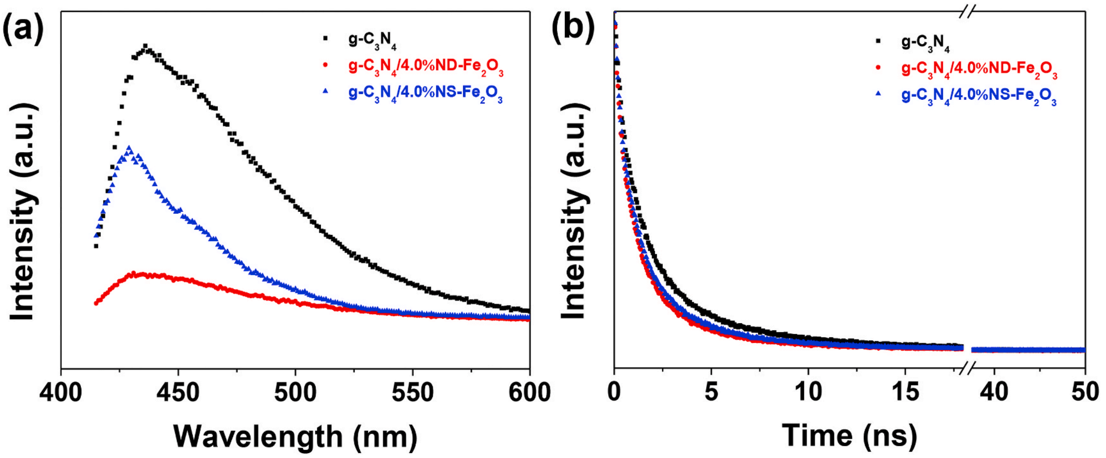

Fig. 6. (a) PL spectra of g-C_3N_4, g-C_3N_4/4.0%ND-Fe_2O_3 and g-C_3N_4/4.0%NS-Fe_2O_3 at the excitation wavelength of 405 nm; (b) TRFD spectra of g-C_3N_4, g-C_3N_4/4.0% ND-Fe_2O_3 and g-C_3N_4/4.0%NS-Fe_2O_3 at the excitation and emission wavelengths of 405 and 435 nm, respectively.

Table 1
The fitted parameters of TRFD spectra over g-C_3N_4, g-C_3N_4/4.0%ND-Fe_2O_3 and g-C_3N_4/4.0NS-Fe_2O_3.

Sample	τ_1 [ns]	B_1	τ_2 [ns]	B_2	τ_3 [ns]	B_3	τ_{ave} [ns]	k_{ET} [ns^{-1}]	η_{inj} [%]	χ^2
g-C_3N_4	0.81	5109	2.77	3815	9.75	661	4.51	–	–	1.212
g-C_3N_4/4.0%ND-Fe_2O_3	0.55	5187	2.00	3961	7.61	538	3.27	0.084	27.5	1.196
g-C_3N_4/4.0%NS-Fe_2O_3	0.66	5469	2.37	3712	8.79	481	3.63	0.054	19.5	1.072

Based on the calculated results (Table 1), it was found that g-C_3N_4/4.0%ND-Fe_2O_3 possessed a higher injection efficiency (≈27.5%) than g-C_3N_4/4.0%NS-Fe_2O_3 (≈19.5%), which was in good accordance with injection rate. These results provided more straightforward and powerful evidence for the more efficient electron transfer between Fe_2O_3 NDs and g-C_3N_4. The efficient electron injection can accelerate the regeneration of surface $\equiv Fe^{2+}$ species, improve the direct activation of H_2O_2 and increase the opportunity of hole oxidation in the photo-Fenton-like process (Wang et al., 2020a,b). All the results based on the EIS, TPC, PL and TRFD measurements revealed that a faster electron injection rate and higher injection efficiency in g-C_3N_4/4.0%ND-Fe_2O_3, probably resulting from the stronger interaction between Fe_2O_3 NDs and g-C_3N_4, brought about the more efficient photo-Fenton-like activity.

Apart from the photoinduced electron transfer between g-C_3N_4 and Fe_2O_3, the interface reactivity between g-C_3N_4/Fe_2O_3 catalyst and reactants (TC and H_2O_2) also played an important role in improving the catalytic activity of g-C_3N_4/Fe_2O_3 in the photo-Fenton-like system. As shown in Fig. 7a, in comparison with g-C_3N_4/4.0%NS-Fe_2O_3, more TC molecules were adsorbed on the surface of g-C_3N_4/4.0%ND-Fe_2O_3, presumably resulting from the homogeneous distribution of Fe_2O_3 NDs which might provide more binding sites and lower steric hindrance toward TC adsorption. Therefore, their opportunities to react with active species at the interface were greatly increased. In addition, generally speaking, to improve the reactivity of a catalyst with H_2O_2 in the photo-Fenton-like system, more H_2O_2 molecules were always anticipated to be activated to •OH radicals (Du et al., 2017; Lima et al., 2017; Yang et al., 2015; Zhao et al., 2020). As a consequence, the generation of •OH radicals over g-C_3N_4/4.0%ND-Fe_2O_3 and g-C_3N_4/4.0%NS-Fe_2O_3 was studied to evaluate their reactivity with H_2O_2. As presented in Fig. 7b, with the increment of reaction time, both the fluorescence peak intensities at ≈430 nm over g-C_3N_4/4.0%ND-Fe_2O_3 and g-C_3N_4/4.0% NS-Fe_2O_3 gradually enhanced in the presence of H_2O_2 under visible light stimulation, demonstrating that an increasing amount of •OH radicals were produced via the photo-Fenton-like reaction (Zhao et al., 2014). In contrast, g-C_3N_4/4.0%ND-Fe_2O_3 showed a higher fluorescence peak intensity than g-C_3N_4/4.0%NS-Fe_2O_3 under the same reaction time, indicating that more H_2O_2 molecules were activated at the interface of g-C_3N_4/4.0%ND-Fe_2O_3. According to these results, we concluded that g-C_3N_4/4.0%ND-Fe_2O_3 showed a stronger interaction with TC and higher reactivity with H_2O_2 at the interface, which further facilitated the improvement of catalytic activity in the photo-Fenton-like process.

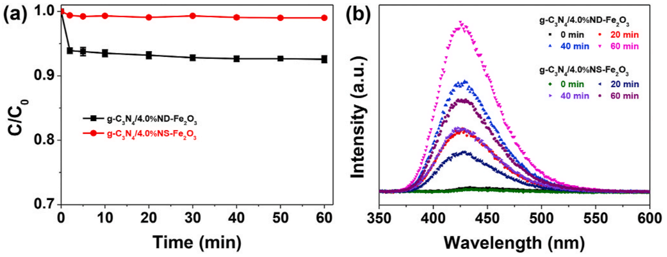

Fig. 7. (a) Adsorption of TC on g-C_3N_4/4.0%ND-Fe_2O_3 and g-C_3N_4/4.0%NS-Fe_2O_3; (b) Fluorescence spectra of g-C_3N_4/4.0%ND-Fe_2O_3 and g-C_3N_4/4.0%NS-Fe_2O_3 with reaction time in the presence of H_2O_2 under visible light stimulation.

Stability was a pivotal factor when considering the practical application of a catalyst. To evaluate the stability of g-C_3N_4/4.0%ND-Fe_2O_3, a time-cycle TC degradation experiment was first performed as presented in Fig. 8a. After four repeated runs, the TC degradation efficiency just reduced by ≈4%, and the chemical and morphological structures of g-C_3N_4/4.0%ND-Fe_2O_3 nearly remained unchanged based on the XRD, FTIR and TEM results (Fig. S13), demonstrating the recycle stability of g-C_3N_4/4.0%ND-Fe_2O_3 in the photo-Fenton-like process. Moreover, the photo-Fenton-like performance of g-C_3N_4/4.0%ND-Fe_2O_3 was studied under different conditions, involving initial pH value changing from 3 to 11, reaction temperature with the varying range of 5–40 °C, as well as the case of ion coexistence including Cl^-, SO_4^{2-}, HCO_3^-, and NO_3^- anions. As displayed in Fig. 8b, all the TC degradation efficiencies changed little, illustrating the robust performance of g-C_3N_4/4.0%ND-Fe_2O_3 in various aquatic environments. Furthermore, it was found that g-C_3N_4/4.0%ND-Fe_2O_3 can use natural solar light to effectively remove TC in the actual tap and river water bodies with both efficiencies of almost ≈95% similar to that in deionized water (Fig. 8c), indicating the potential practical

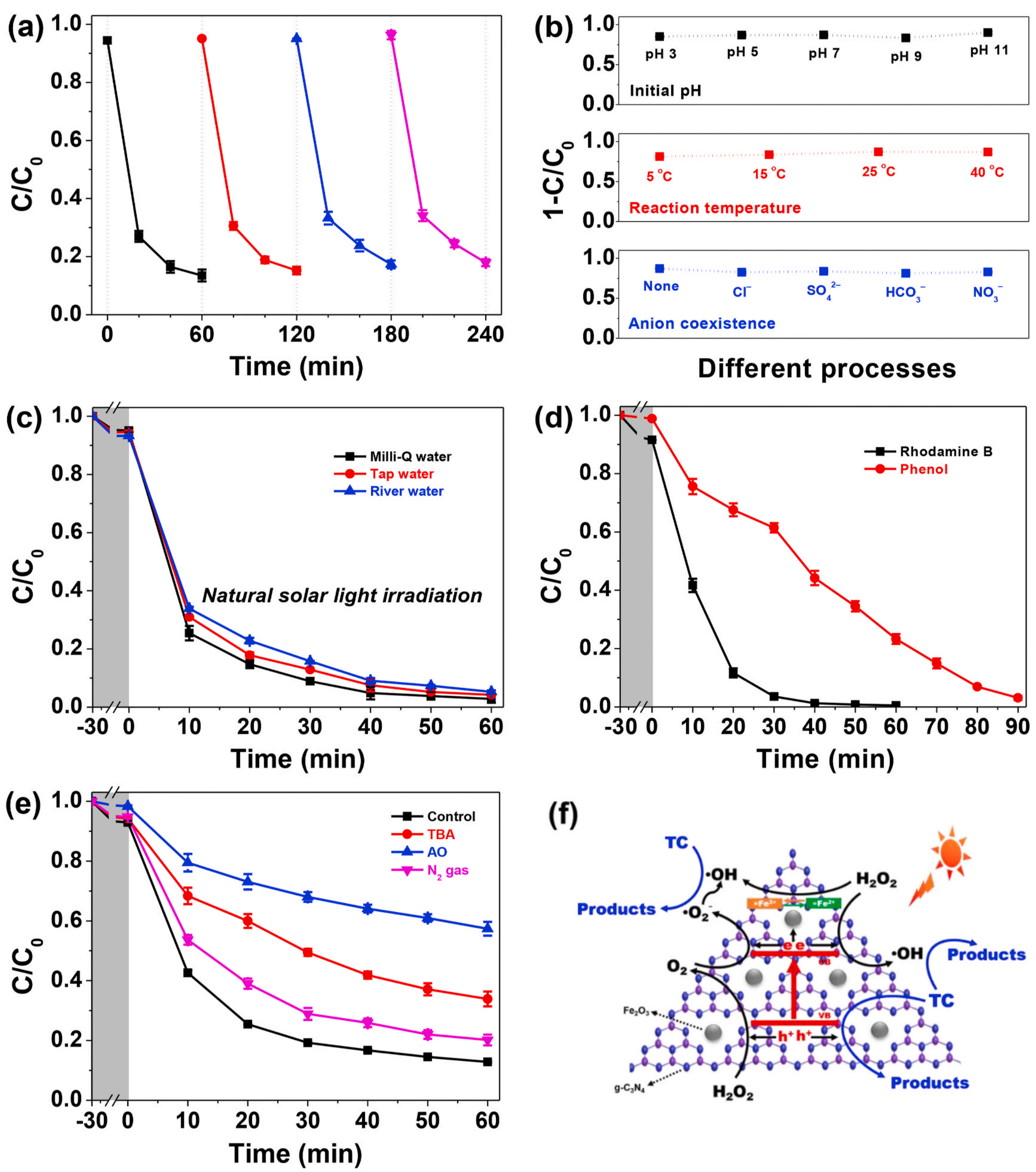

Fig. 8. (a) Photo-Fenton-like TC degradation by $g-C_3N_4/4.0\%ND-Fe_2O_3$ in the recycle experiment; (b) Effect of initial pH, reaction temperature and anion existence on photo-Fenton-like TC degradation efficiency by $g-C_3N_4/4.0\%ND-Fe_2O_3$; (c) Natural sunlight driven TC degradation activity by $g-C_3N_4/4.0\%ND-Fe_2O_3$ in tap water and river water (outdoor was sunny with the temperature of 25–29 °C); (d) Photo-Fenton-like degradation of rhodamine B and phenol by $g-C_3N_4/4.0\%ND-Fe_2O_3$; (e) Effect of the presence of TBA, AO and N_2 gas on photo-Fenton-like activity of $g-C_3N_4/4.0\%ND-Fe_2O_3$ for TC degradation; (f) Schematic diagram of photo-Fenton-like TC degradation by $g-C_3N_4/4.0\%ND-Fe_2O_3$.

application of $g-C_3N_4/4.0\%ND-Fe_2O_3$ to remedy real antibiotic wastewaters via utilizing natural solar light. In addition to these, we noticed that the reflection to the efficient activity of $g-C_3N_4/4.0\%ND-Fe_2O_3$ was not limited to TC contaminant. Other refractory pollutants including rhodamine B and phenol can be also efficiently degraded. As seen from Fig. 8d, all the rhodamine B molecules could be degraded within 40 min under the same experimental condition while over ≈96% for phenol after 90 min H_2O_2 concentration (10–70 mM) also affected the TC degradation (Fig. S14). When the concentration of H_2O_2 increased from 10 to 50 mM, the peak TC degradation rate and efficiency were acquired. However, further increase of H_2O_2 concentration (70 mM) resulted in the declined activity, probably due to the excessive H_2O_2 maybe as the scavengers for reactive oxidation species such as hydroxyl radicals (Cheng et al., 2018). However, at least ≈83% of TC molecules can be degraded. All of these results well demonstrated the efficient and robust performance of $g-C_3N_4/4.0\%ND-Fe_2O_3$ in the photo-Fenton-like process. The primary active oxide species responsible for TC degradation were determined by a common radical-trapping strategy. The ammonium oxalate (AO), *tert*-butyl alcohol (TBA), and nitrogen gas (N_2) were employed as the specific scavengers for the photogenerated holes, •OH and $\bullet O_2^-$ radicals, respectively (Zhao et al., 2020). As presented in Fig. 8e and Fig. S15, as we expected, the addition of TBA suppressed the TC degradation with efficiency and rate declining from ≈87% and ≈0.037 min^{-1} to ≈66% and ≈0.020 min^{-1}, indicating that •OH radicals acted as a typical active species for TC degradation. Moreover, when AO and N_2 gas were selectively added, the performances of $g-C_3N_4/4.0\%ND-Fe_2O_3$ also suffered the inhibition and the TC degradation efficiencies and rates decreased to ≈43% and ≈0.010 min^{-1} as well as ≈80% and ≈0.033

min^{-1}, respectively. These results demonstrated that both the photogenerated holes and $\bullet O_2^-$ radicals also played an important role in the removal of TC. In addition, the valence band (VB) and conduction band (CB) edges of g-C_3N_4 nanosheets were determined to be 1.68 and −1.28 V *vs.* NHE, respectively (Table S2). According to these findings, the possible TC degradation pathways in the g-C_3N_4/4.0%ND-Fe_2O_3 photo-Fenton-like system were proposed as shown in Fig. 8f: (i) Since the photogenerated electrons were rapidly injected from CB of g-C_3N_4 to Fe_2O_3 NDs, the regeneration of surface $\equiv Fe^{2+}$ species from Fe^{3+} reduction ($Fe^{3+}/Fe^{2+} = 0.77$ V *vs.* NHE) were accelerated which facilitated the transformation of H_2O_2 into $\bullet OH$ radicals, leading to the removal of TC; (ii) These electrons also can be captured by H_2O_2, directly resulting in the formation of $\bullet OH$ radicals ($H_2O_2/\bullet OH = 1.14$ V *vs.* NHE (Nosaka and Nosaka, 2017)) to make TC be degraded; (iii) The photogenerated holes in VB of g-C_3N_4 can be directly used as an active species to remove TC; (iv) These holes also can oxidize H_2O_2 molecules to continuously generate dissolved O_2 ($H_2O_2/O_2 = 0.695$ V *vs.* NHE (Nosaka and Nosaka, 2017)), that can be reduced by photogenerated electrons bringing about the production of $\bullet O_2^-$ ($O_2/\bullet O_2^- = -0.33$ V *vs.* NHE) radicals for TC degradation; And (v) these formed $\bullet O_2^-$ radicals also can convert to $\bullet OH$ radicals to degrade TC (Dong et al., 2014). The degradation intermediates of TC are identified by LC-MS technology and the possible structures of the products are elucidated. As presented in Fig. S16, the TC peaks at retention time of 4.94 min and 5.51 min decreased with the process of the reaction. The main product peaks appeared at 0.76, 1.15, 5.26, 5.87 and 6.02 min in the degradation process. According to the analyses of mass spectra (Table S3), products with m/z of 282.2, 223.1, 460.2 and 441.1 were determined and the corresponding structures were proposed.

4. Conclusions

To sum up, simple synthetic processes were developed to obtain g–C_3N_4–based hybrid catalysts with different morphological Fe_2O_3 containing NDs and NSs. Compared with Fe_2O_3 NSs, a stronger interaction between Fe_2O_3 NDs and g-C_3N_4 was observed at the interface. The visible-light-driven photo-Fenton-like activity showed that g-C_3N_4/4.0%ND-Fe_2O_3 heterojunction exhibited higher TC removal efficiency and rate (≈87% and ≈0.037 min^{-1}) than g-C_3N_4/4.0%NS-Fe_2O_3 counterpart (≈57% and ≈0.016 min^{-1}). The faster electron injection rate and higher injection efficiency (≈0.084 ns^{-1} and ≈27.5%) in g-C_3N_4/4.0% ND-Fe_2O_3 contrast to g-C_3N_4/4.0%NS-Fe_2O_3 (≈0.054 ns^{-1} and ≈19.5%), resulting from the stronger interfacial interaction between Fe_2O_3 NDs and g-C_3N_4, brought about more efficient photo-Fenton-like activity. On the other hand, g-C_3N_4/4.0%ND-Fe_2O_3 also displayed stronger interaction with TC and higher reactivity with H_2O_2 which further facilitated the improvement of catalytic activity. Furthermore, we found that g-C_3N_4/4.0%ND-Fe_2O_3 can remain robust performances under different conditions. Therefore, this *in-situ* deposited g-C_3N_4/ND-Fe_2O_3 hybrid preformed great potential for photo-Fenton-like purification of antibiotic wastewaters.

Declaration of competing interest

The authors declare that they have no known competing financial interests or personal relationships that could have appeared to influence the work reported in this paper.

Acknowledgements

This study is supported by the National Natural Science Foundation of China (No. 21806059), Natural Science Foundation of Jiangsu Higher Education Institution (No. 17KJB610006), China Postdoctoral Science Foundation (No. 2018M630524), Hong Kong Scholars Program of Society of Hong Kong Scholars (No. XJ2018031), Research Grant Council, University Grants Council (No. GRF14100115) and Technology and Business Development Fund, The Chinese University of Hong Kong (No. TBF18SCI006).

Appendix A. Supplementary data

Supplementary data to this article can be found online at https://doi.org/10.1016/j.envres.2021.110842.

References

Abdellah, M., Žídek, K., Zheng, K., Chábera, P., Messing, M.E., Pullerits, T., 2013. Balancing electron transfer and surface passivation in gradient CdSe/ZnS core-shell quantum dots attached to ZnO. J. Phys. Chem. Lett. 4, 1760–1765. https://doi.org/10.1021/jz4006459.

Andreozzi, R., Caprio, V., Insola, A., Marotta, R., 1999. Advanced oxidation processes (AOP) for water purification and recovery. Catal. Today 53, 51–59. https://doi.org/10.1016/S0920-5861(99)00102-9.

Chen, L., Yang, X., Chen, J., Liu, J., Wu, H., Zhan, H., Liang, C., Wu, M., 2010. Continuous shape- and spectroscopy-tuning of hematite nanocrystals. Inorg. Chem. 49, 8411–8420. https://doi.org/10.1021/ic100919a.

Chen, C.Q., Zheng, L., Zhou, J.L., Zhao, H., 2017. Persistence and risk of antibiotic residues and antibiotic resistance genes in major mariculture sites in Southeast China. Sci. Total Environ. 580, 1175–1184. https://doi.org/10.1016/j.scitotenv.2016.12.075.

Cheng, M., Zeng, G., Huang, D., Lai, C., Liu, Y., Zhang, C., Wan, J., Hu, L., Zhou, C., Xiong, W., 2018. Efficient degradation of sulfamethazine in simulated and real wastewater at slightly basic pH values using Co-SAM-SCS/H_2O_2 Fenton-like system. Water Res. 138, 7–18. https://doi.org/10.1016/j.watres.2018.03.022.

Clarizia, L., Russoa, D., Somma, I.D., Marotta, R., Andreozzi, R., 2017. Homogeneous photo-Fenton processes at near neutral pH: a review. Appl. Catal. B Environ. 209, 358–371. https://doi.org/10.1016/j.apcatb.2017.03.011.

Dong, F., Wang, Z., Li, Y., Ho, W., Lee, S.C., 2014. Immobilization of polymeric g-C_3N_4 on structured ceramic foam for efficient visible light photocatalytic air purification with real indoor illumination. Environ. Sci. Technol. 48, 10345–10353. https://doi.org/10.1021/es502290f.

Du, D., Shi, W., Wang, L., Zhang, J., 2017. Yolk-shell structured Fe_3O_4@void@TiO_2 as a photo-Fenton-like catalyst for the extremely efficient elimination of tetracycline. Appl. Catal. B Environ. 200, 484–492.

Fu, J., Yu, J., Jiang, C., Cheng, B., 2017. g-C_3N_4-based heterostructured photocatalysts. Adv. Energy Mater. 8, 1701503. https://doi.org/10.1002/aenm.201701503.

Gao, H., Yang, H., Xu, J., Zhang, S., Li, J., 2018. Strongly coupled g-C_3N_4 nanosheets-Co_3O_4 quantum dots as 2D/0D heterostructure composite for peroxymonosulfate activation. Small 14, 1801353. https://doi.org/10.1002/smll.201801353.

Ge, L., Zuo, F., Liu, J., Ma, Q., Wang, C., Sun, D., Bartels, L., Feng, P., 2012. Synthesis and efficient visible light photocatalytic hydrogen evolution of polymeric g-C_3N_4 coupled with CdS quantum dots. J. Phys. Chem. C 116, 13708–13714. https://doi.org/10.1021/jp3041692.

Guo, H., Chen, M., Zhong, Q., Wang, Y., Ma, W., Ding, J., 2019a. Synthesis of Z-scheme α-Fe_2O_3/g-C_3N_4 composite with enhanced visible light photocatalytic reduction of CO_2 to CH_3OH. J. CO_2 Utilization 33, 233–241. https://doi.org/10.1016/j.jcou.2019.05.016.

Guo, T., Wang, K., Zhang, G., Wu, X., 2019b. A novel α-Fe_2O_3@g-C_3N_4 catalyst: synthesis derived from Fe-based MOF and its superior photo-Fenton performance. Appl. Surf. Sci. 469, 331–339. https://doi.org/10.1016/j.apsusc.2018.10.183.

Han, Q., Wang, B., Zhao, Y., Hu, C., Qu, L., 2015. A graphitic-C_3N_4 "seaweed" architecture for enhanced hydrogen evolution. Angew. Chem. Int. Ed. 54, 11433–11477. https://doi.org/10.1002/ange.201504985.

Herney-Ramireza, J., Vicenteb, M.A., Madeira, L.M., 2010. Heterogeneous photo-Fenton oxidation with pillared clay-based catalysts for wastewater treatment: a review. Appl. Catal. B Environ. 98, 10–26. https://doi.org/10.1016/j.apcatb.2010.05.004.

Jiang, D.L., Li, J., Xing, C.S., Zhang, Z.Y., Meng, S., Chen, M., 2015. Two-dimensional $CaIn_2S_4$/g-C_3N_4 heterojunction nanocomposite with enhanced visible-light photocatalytic activities: interfacial engineering and mechanism insight. ACS Appl. Mater. Interfaces 7, 19234–19242. https://doi.org/10.1021/acsami.5b05118.

Jiang, Z., Wan, W., Li, H., Yuan, S., Zhao, H., Wong, P.K., 2018. A hierarchical Z-scheme α-Fe_2O_3/g-C_3N_4 hybrid for enhanced photocatalytic CO_2 reduction. Adv. Mater. 30, 1706108. https://doi.org/10.1002/adma.201706108.

Jiang, L., Wang, K., Wu, X., Zhang, G., 2020. Highly enhanced full solar spectrum-driven photocatalytic CO_2 reduction performance in $Cu_{2-x}S$/g-C_3N_4 composite: efficient charge transfer and mechanism insight. Solar RRL 5, 2000326. https://doi.org/10.1002/solr.202000326.

Li, C., Du, Y., Wang, D., Yin, S., Tu, W., Chen, Z., Kraft, M., Chen, G., Xu, R., 2017a. Unique P-Co-N surface bonding states constructed on g-C_3N_4 nanosheets for drastically enhanced photocatalytic activity of H_2 Evolution. Adv. Funct. Mater. 27, 1604328. https://doi.org/10.1002/adfm.201604328.

Li, N., Zhang, J., Tian, Y., Zhao, J., Zhang, J., Zuo, W., 2017b. Precisely controlled fabrication of magnetic 3D γ-Fe_2O_3@ZnO core-shell photocatalyst with enhanced activity: ciprofloxacin degradation and mechanism insight. Chem. Eng. J. 308, 377–385. https://doi.org/10.1016/j.cej.2016.09.093.

Lima, M.J., Silva, C.G., Silva, A.M.T., Lopes, J.C.B., Dias, M.M., Faria, J.L., 2017. Homogeneous and heterogeneous photo-Fenton degradation of antibiotics using an innovative static mixer photoreactor. Chem. Eng. J. 310, 342–351. https://doi.org/10.1016/j.cej.2016.04.032.

Liu, J., Zheng, M., Shi, X., Zeng, H., Xia, H., 2016. Amorphous FeOOH quantum dots assembled mesoporous film anchored on graphene nanosheets with superior electrochemical performance for supercapacitors. Adv. Funct. Mater. 26, 919–930. https://doi.org/10.1002/adfm.201504019.

Liu, J., Yu, Y., Qia, R., Cao, C., Liu, X., Zheng, Y., Song, W., 2019. Enhanced electron separation on in-plane benzene-ring doped g-C_3N_4 nanosheets for visible light photocatalytic hydrogen evolution. Appl. Catal. B Environ. 244, 459–464. https://doi.org/10.1016/j.apcatb.2018.11.070.

Miklos, D.B., Remy, C., Jekel, M., Linden, K.G., Drewes, J.E., Hübner, U., 2018. Evaluation of advanced oxidation processes for water and wastewater treatment e A critical review. Water Res. 139, 118–131. https://doi.org/10.1016/j.watres.2018.03.042.

Nosaka, Y., Nosaka, A.Y., 2017. Generation and detection of reactive oxygen species in photocatalysis. Chem. Rev. 117, 11302–11336. https://doi.org/10.1021/acs.chemrev.7b00161.

Ong, W., Tan, L., Ng, Y.H., Yong, S., Chai, S., 2016. Graphitic carbon nitride (g-C_3N_4)-based photocatalysts for artificial photosynthesis and environmental remediation: are we a step closer to achieving sustainability? Chem. Rev. 116, 7159–7329. https://doi.org/10.1021/acs.chemrev.6b00075.

Pouran, S.R., Aziz, A.R.A., Daud, W.M.A.W., 2015. Review on the main advances in photo-Fenton oxidation system for recalcitrant wastewaters. J. Ind. Eng. Chem. 21, 53–69. https://doi.org/10.1016/j.jiec.2014.05.005.

Ran, J., Zhang, J., Yu, J., Jaroniec, M., Qiao, S.Z., 2014. Earth-abundant cocatalysts for semiconductor based photocatalytic water splitting. Chem. Soc. Rev. 43, 7787–7812. https://doi.org/10.1039/C3CS60425J.

Shi, X., Fujitsuka, M., Kim, S., Majima, T., 2018. Faster electron injection and more active sites for efficient photocatalytic H_2 evolution in g-C_3N_4/MoS_2 hybrid. Small 14, 1703277. https://doi.org/10.1002/smll.201703277.

Su, Y., Wu, Z., Wu, Y., Yu, J., Sun, L., Lin, C., 2015. Acid Orange II degradation through a heterogeneous Fenton-like reaction using Fe-TiO_2 nanotube arrays as a photocatalyst. J. Mater. Chem. A 3, 8537–8544. https://doi.org/10.1039/C5TA00839E.

Trovo, G., Nogueira, R.F.P., Aguera, A., Fernandez-Alba, A.R., Malato, S., 2011. Degradation of the antibiotic amoxicillin by photo Fenton process-chemical and toxicological assessment. Water Res. 45, 1394–1402. https://doi.org/10.1016/j.watres.2010.10.029.

Wang, M.Q., Yang, W.H., Wang, H.H., Chen, C., Zhou, Z.Y., Sun, S.G., 2014. Pyrolyzed Fe-N-C composite as an efficient non-precious metal catalyst for oxygen reduction reaction in acidic medium. ACS Catal. 4, 3928–3936. https://doi.org/10.1021/cs500673k.

Wang, H.X., Wang, N., Wang, B., Zhao, Q., Fang, H., Fu, C.W., Tang, C.X., Jiang, F., Zhou, Y., Chen, Y., Jiang, Q.W., 2016. Antibiotics in drinking water in Shanghai and their contribution to antibiotic exposure of school children. Environ. Sci. Technol. 50, 2692–2699. https://doi.org/10.1021/acs.est.5b05749.

Wang, K., Jiang, L., Wu, X., Zhang, G., 2020a. Vacancy mediated Z-scheme charge transfer in a 2D/2D $La_2Ti_2O_7$/g-C_3N_4 nanojunction as a bifunctional photocatalyst for solar-to-energy conversion. J. Mater. Chem. A 8, 13241–13247. https://doi.org/10.1039/D0TA01310B.

Wang, X., Zhang, X., Zhang, Y., Wang, Y., Sun, S., Wu, W.D., Wu, Z., 2020b. Nanostructured semiconductor supported iron catalysts for heterogeneous photo-Fenton oxidation: a review. J. Mater. Chem. A 8, 15513–15546. https://doi.org/10.1039/D0TA04541A.

Xi, J., Xia, H., Ning, X., Zhang, Z., Liu, J., Mu, Z., Zhang, S., Du, P., Lu, X., 2019. Carbon-intercalated 0D/2D hybrid of hematite quantum dots/graphitic carbon nitride nanosheets as superior catalyst for advanced oxidation. Small 43, 1902744. https://doi.org/10.1002/smll.201902744.

Xu, J., Wang, Z., Zhu, Y., 2017. Enhanced visible-light-driven photocatalytic disinfection performance and organic pollutants degradation activity of porous g-C_3N_4 nanosheets. ACS Appl. Mater. Interfaces 9, 27727–27735. https://doi.org/10.1021/acsami.7b07657.

Xue, J., Ma, S., Zhou, Y., Zhang, Z., He, M., 2015. Facile photochemical synthesis of Au/Pt/g-C_3N_4 with plasmon-enhanced photocatalytic activity for antibiotic degradation. ACS Appl. Mater. Interfaces 7, 9630–9637. https://doi.org/10.1021/acsami.5b01212.

Yan, M., Hua, Y.Q., Zhu, F.F., Gu, W., Jiang, J.H., Shen, H.Q., Shi, W.D., 2017. Fabrication of nitrogen doped graphene quantum dots-BiOI/$MnNb_2O_6$ pn junction photocatalysts with enhanced visible light efficiency in photocatalytic degradation of antibiotics. Appl. Catal. B Environ. 202, 518–527. https://doi.org/10.1016/j.apcatb.2016.09.039.

Yang, X., Chen, W., Huang, J., Zhou, Y., Zhu, Y., Li, C., 2015. Rapid degradation of methylene blue in a novel heterogeneous Fe_3O_4@rGO@TiO_2-catalyzed photo-Fenton system. Sci. Rep. 5, 10632. https://doi.org/10.1038/srep10632.

Ye, M.Y., Zhao, Z.H., Hu, Z.F., Liu, L.Q., Ji, H.M., Shen, Z.R., Ma, T.Y., 2017. 0D/2D heterojunctions of vanadate quantum dots/graphitic carbon nitride nanosheets for enhanced visible-light-driven photocatalysis. Angew. Chem. Int. Ed. 56, 8407–8411. https://doi.org/10.1002/anie.201611127.

Zhang, J., Zhang, M., Zhang, G., Wang, X., 2012. Synthesis of carbon nitride semiconductors in sulfur flux for water photoredox catalysis. ACS Catal. 2, 940–948. https://doi.org/10.1021/cs300167b.

Zhang, Z.Y., Huang, J.D., Zhang, M.Y., Yuan, L., Dong, B., 2015. Ultrathin hexagonal SnS_2 nanosheets coupled with g-C_3N_4 nanosheets as 2D/2D heterojunction photocatalysts toward high photocatalytic activity. Appl. Catal. B Environ. 163, 298–305. https://doi.org/10.1016/j.apcatb.2014.08.013.

Zhang, K., Liu, Y., Deng, J., Xie, S., Lin, H., Zhao, X., Yang, J., Han, Z., Dai, H., 2017. Fe_2O_3/3DOM $BiVO_4$: high-performance photocatalysts for the visible light-driven degradation of 4-nitrophenol. Appl. Catal. B Environ. 202, 569–579. https://doi.org/10.1016/j.apcatb.2016.09.069.

Zhao, H., Dong, Y., Jiang, P., Wang, G., Zhang, J., Li, K., 2014. An insight into the kinetics and interface sensitivity for catalytic ozonation: the case of nano-sized $NiFe_2O_4$. Catal. Sci. Technol. 4, 494–501. https://doi.org/10.1039/C3CY00674C.

Zhao, H., Tian, C., Mei, J., Yang, S., Wong, P.K., 2020. Synergistic effect and mechanism of catalytic degradation toward antibiotic contaminants by amorphous goethite nanoparticles decorated graphitic carbon nitride. Chem. Eng. J. 390, 124551. https://doi.org/10.1016/j.cej.2020.124551.

Zhao, H., Jiang, Z., Xiao, K., Sun, H., Chan, H.S., Tsang, T.H., Yang, S., Wong, P.K., 2021. Photo-assisted separation of noble-metal-free oxidation and reduction cocatalysts for graphitic carbon nitride nanosheets with efficient photocatalytic hydrogen evolution. Appl. Catal. B Environ. 280, 119456. https://doi.org/10.1016/j.apcatb.2020.119456.

Zhen, W., Ning, X., Yang, B., Wu, Y., Li, Z., Lu, G., 2018. The enhancement of CdS photocatalytic activity for water splitting via anti-photocorrosion by coating Ni_2P shell and removing nascent formed oxygen with artificial gill. Appl. Catal. B Environ. 221, 243–257. https://doi.org/10.1016/j.apcatb.2017.09.024.

Zhu, J., Yin, Z., Yang, D., Sun, T., Yu, H., Hoster, H., Hng, H., Zhang, H., Yan, Q., 2013. Hierarchical hollow spheres composed of ultrathin Fe_2O_3 nanosheets for lithium storage and photocatalytic water oxidation. Energy Environ. Sci. 6, 987–993. https://doi.org/10.1039/C2EE24148J.